Journal of Materials Chemistry B

ROYAL SOCIETY OF CHEMISTRY

PAPER

View Article Online
View Journal | View Issue

Cite this: J. Mater. Chem. B, 2024, 12, 5360

Bioprinted biomimetic hydrogel matrices guiding stem cell aggregates for enhanced chondrogenesis and cartilage regeneration†

Yuetian Liu,‡[ab] Lijuan Du,‡[b] Hua Zhang,*[bd] Guanrong Li,[ab] Yang Luo,[ab] Zeming Hu,[b] Rong Xu,[ab] Jie Yao,[a] Zheyuan Shi,[ab] Yige Chen,[b] Chi Zhang,[a] Zhanping Jin,[a] Caihua Zhang,[a] Chanchan Xie,[a] Jun Fu,*[c] Yabin Zhu*[b] and Yingchun Zhu*[a]

Articular cartilage tissue has limited self-repair capabilities, with damage frequently progressing to irreversible degeneration. Engineered tissues constructed through bioprinting and embedded with stem cell aggregates offer promising therapeutic alternatives. Aggregates of bone marrow mesenchymal stromal cells (BMSCs) demonstrate enhanced and more rapid chondrogenic differentiation than isolated cells, thus facilitating cartilage repair. However, it remains a key challenge to precisely control biochemical microenvironments to regulate cellular adhesion and cohesion within bioprinted matrices simultaneously. Herein, this work reports a bioprintable hydrogel matrix with high cellular adhesion and aggregation properties for cartilage repair. The hydrogel comprises an enhanced cell-adhesive gelatin methacrylate and a cell-cohesive chitosan methacrylate (CHMA), both of which are subjected to photo-initiated crosslinking. By precisely adjusting the CHMA content, the mechanical stability and biochemical cues of the hydrogels are finely tuned to promote cellular aggregation, chondrogenic differentiation and cartilage repair implantation. Multi-layer constructs encapsulated with BMSCs, with high cell viability reaching 91.1%, are bioprinted and photo-crosslinked to support chondrogenic differentiation for 21 days. BMSCs rapidly form aggregates and display efficient chondrogenic differentiation both on the hydrogels and within bioprinted constructs, as evidenced by the upregulated expression of Sox9, Aggrecan and Collagen 2a1 genes, along with high protein levels. Transplantation of these BMSC-laden bioprinted hydrogels into cartilaginous defects demonstrates effective hyaline cartilage repair. Overall, this cell-responsive hydrogel scaffold holds immense promise for applications in cartilage tissue engineering.

Received 17th February 2024,
Accepted 22nd April 2024

DOI: 10.1039/d4tb00323c

rsc.li/materials-b

1. Introduction

Articular cartilage is an avascular and abneural connective tissue comprised of superficial individual chondrocytes and deeper aggregated chondrocytes distributed in the extracellular matrix (ECM). Traumas, diseases, and the natural aging process often lead to articular cartilage damage. Unfortunately, its inherent limited capacity for self-repair poses significant challenges in terms of its repair and reconstruction.[1] In the realm of clinical practice, current methods employed for articular cartilage repair presently encompass autologous cartilage transplantation,[2] artificial joint replacement,[3] intra-articular administration of autologous bone marrow mesenchymal stem cells,[4] and autologous platelet-rich plasma.[5] Although these strategies have attained great success, limitations remain, including the scarcity of available donor tissue, the intricate nature of surgical procedures, and the finite durability of prosthetic materials. Consequently, there exists an urgent requirement for a feasible, biocompatible, and regenerative approach aimed at addressing articular cartilage defects.

Numerous studies have demonstrated the potential of polymer hydrogels in facilitating the repair of articular cartilage defects, owing to their excellent biocompatibility, water

[a] The First Affiliated Hospital of Ningbo University, Ningbo, Zhejiang 315010, China. E-mail: fyyzhuyingchun@nbu.edu.cn
[b] Research Institute of Smart Medicine and Biological Engineering, Health Science Center, Ningbo University, Ningbo, Zhejiang 315211, China. E-mail: zhanghua@nbu.edu.cn, zhuyabin@nbu.edu.cn
[c] Key Laboratory of Polymeric Composite and Functional Materials of Ministry of Education, Guangdong Engineering Technology Research Centre for Functional Biomaterials, School of Materials Science and Engineering, Sun Yat-Sen University, Guangzhou, 510275, China. E-mail: fujun8@mail.sysu.edu.cn
[d] State Key Laboratory of Molecular Engineering of Polymers (Fudan University), Shanghai 200438, China

† Electronic supplementary information (ESI) available. See DOI: https://doi.org/10.1039/d4tb00323c

‡ These authors contributed equally to this work.

retention capabilities, and ability to emulate natural cartilage tissue characteristics.[6–8] Leveraging the tunability and plasticity of hydrogel materials, researchers have successfully bioprinted biomimetic scaffolds in the defect area, providing favorable conditions for the growth of stem cells and chondrogenic differentiation.[9–11] Moreover, in comparison to individual stem cells distributed in the hydrogels, encapsulating cell spheroids or micro-aggregates within bioprinted hydrogels are more conducive to chondrogenic differentiation and cartilage repair.[12–14] Similarly, in the deep matrix of articular cartilage, multiple chondrocytes are located within the cartilage traps.[15] These chondrocytes actively contribute to maintaining tissue integrity, synthesizing the ECM, responding to mechanical cues, and actively participating in repair processes.[16] Therefore, numerous efforts have been directed towards developing a biomimetic hydrogel matrix to induce cell micro-aggregation. One typical strategy involves maximizing cell-to-cell contact while minimizing cellular adhesion to hydrogels to achieve cellular micro-aggregates.[17] Specifically, low-adhesive hydrogels made from polyethylene glycol, polyvinyl alcohol, and alginate have been developed as optimal biomimetic extracellular matrices.[18,19] Nonetheless, low-adhesive hydrogel scaffolds often lack the biological activity inherent in natural matrices, thereby leading to a diminished long-term cell survival rate.[20]

In addition to low-adhesive polymers, chitosan has been found to improve the calcium binding capacity of the substrate and up-regulate the *N*-cadherin adhesion molecule, facilitating stem cells into spheroids.[21,22] Moreover, it is remarkable that the cellular spheroids on chitosan-based scaffolds exhibited long-term proliferation and high chondrogenic differentiation efficiency.[23] Various chitosan-based coatings, films, and nanofiber sponges have been prepared for improving the formation of cell spheroids due to the biological signaling function of chitosan.[24,25] However, since the cells on chitosan substrates are very motile during the assembly of multicellular spheroids, these scaffolds showed limited adhesion of chondrocytes and stem cells, potentially resulting in diminished differentiation and compromised efficacy in cartilage repair processes.

Cell interactions with the ECM and neighboring cells are mediated by integrins and cadherins at the level of the plasma membrane, respectively.[26,27] Integrins and cadherins are intrinsically linked through the actin cytoskeleton and share some signaling molecules to control the proliferation, differentiation and survival of cells.[28] Consequently, incorporating chitosan with other molecules containing adhesion motifs could enhance the adhesiveness of cellular spheroids on chitosan-based scaffolds.[29] For example, Lin *et al.* showcased that a chitosan-cartilage extracellular matrix composite scaffold significantly enhanced the adhesiveness of cellular spheroids, thus efficiently inducing the chondrogenic differentiation of adipose-derived stem cells.[30] Our group recently developed a bioactive chitosan-based hydrogel by introducing polysaccharide xyloglucan into chitosan methacrylate.[31] This scaffold elicited a distinctive cellular response, effectively modulating the formation of cell spheroids. Moreover, these cell spheroids exhibited sustained growth, indicative of robust viability. While these studies provided valuable insights into enhancing the chondrogenic differentiation of stem cells and promote cartilage repair through the simultaneous improvement of cell attachment and micro-aggregation on chitosan-based scaffolds, the exploration of the chitosan composite hydrogels concerning stem cell response, chondrogenic differentiation and cartilage repair remains relatively limited.

In this study, we developed a bioprintable composite hydrogel with a remarkable cell-aggregation response for articular cartilage repair, composed of a high cell-cohesive chitosan methacrylate (CHMA) and an enhanced cell-adhesive gelatin methacrylate (GelMA) (Scheme 1a). Consequently, the combination of GelMA and CHMA networks through one-step photocrosslinking can concurrently modulate the cellular adhesiveness and aggregation properties of the hydrogels (Scheme 1b). The GelMA concentration was purposefully sustained at 10 wt%, a concentration previously reported for developing hydrogels with high cyto-activity and bioadaptability for cartilage engineering.[32–34] Through precise modulation of the CHMA ratio from 0.5 wt% to 1.5 wt%, it was possible to adeptly fine-tune the mechanical and biochemical micro-environments of the resulting hydrogels. The designed composite hydrogels substantially promote the formation of micro-aggregates and facilitate the chondrogenic differentiation of bone marrow-derived mesenchymal stem cells (BMSCs), both on the hydrogel surfaces (Scheme 1c) and within the bioprinted multi-layered constructs (Scheme 1d and e). The efficacy of the bioprinted hydrogel laden with BMSCs on a cartilage injury model was comprehensive investigated, showing successful tissue repair (Scheme 1f). The results demonstrated that this bioprinted cell-adhesion responsive composite hydrogel embedded with BMSCs holds clinical promise for cartilage tissue regeneration application.

2. Materials and methods

2.1 Materials

Chitosan (viscosity: 100–200 mPa s, degree of deacetylation: ≈95%), methacrylic anhydride (MA, 94%), acetic acid (99.8%), gelatin, lithium phenyl (2,4,6-trimethylbenzoyl)phosphinate (LAP) and dialysis tubing with a cutoff molecular weight of 8–14 kDa were purchased from Aladdin (Shanghai, China). Dulbecco's modified Eagle's medium (DMEM) and the chondrogenic induction differentiation medium were sourced from Pricella (USA). Fetal bovine serum (FBS) and penicillin/streptomycin were obtained from Gibco (USA). Calcein-AM/PI were acquired from BeyoGold (Shanghai, China). FITC-phalloidin was purchased from UElandy (Suzhou, China). Collagen Type II and a rabbit monoclonal antibody against Type II Collagen were sourced from Proteintech (Wuhan, China). A rabbit monoclonal antibody against aggrecan was obtained from Affinity (Jiangsu, China). Horseradish peroxidase-conjugated anti-rabbit antibody was procured from Dako (Denmark). Diaminobenzidine tetrahydrochloride (DAB) was purchased from Yeasen (Shanghai, China). Immunohistochemical CD68 was acquired from Servicebio (Wuhan, China).

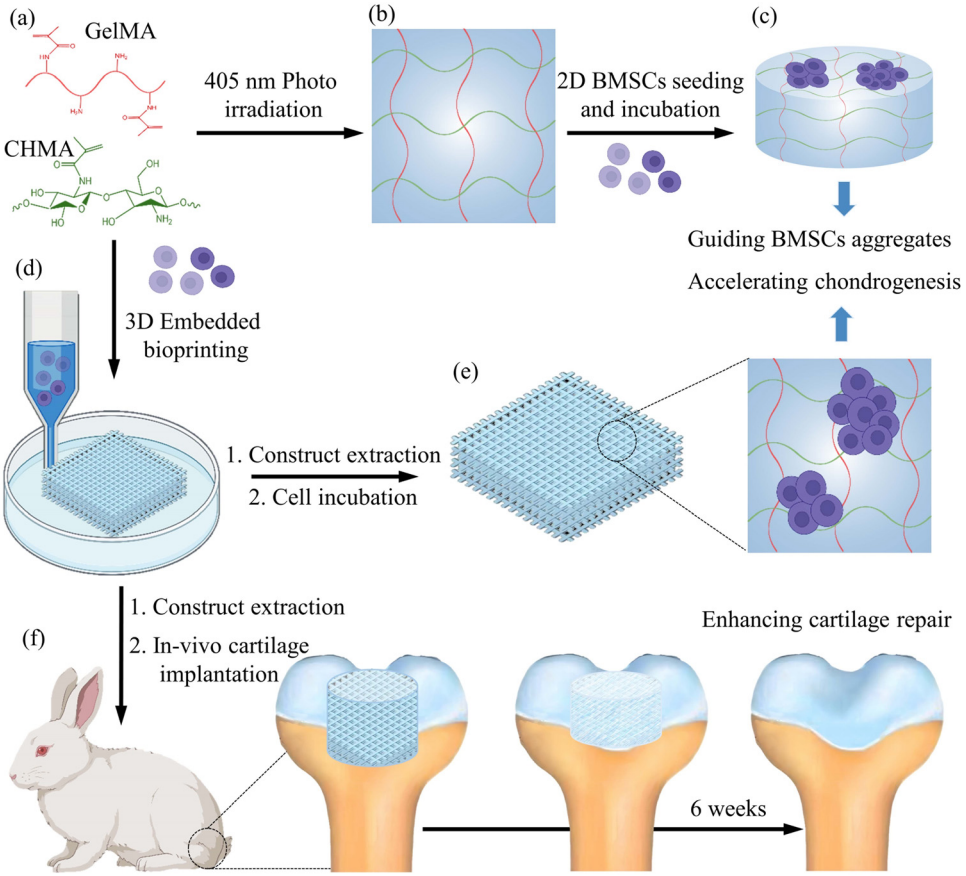

Scheme 1 Construction of cell-adhesion responsive biomimetic hydrogel matrices for articular cartilage repair. (a) and (b) Illustration of the chemical structures (a) of GelMA and CHMA and their photopolymerized hydrogel network (b). (c) Promotion of bone marrow mesenchymal stromal cells (BMSCs) microaggregate growth and chondrogenic differentiation on the hydrogel. (d) Embedded 3D-bioprinting of BMSC-laden hydrogels. (e) BSMC microaggregate growth and chondrogenic differentiation within bioprinted hydrogels. (f) Application of bioprinted hydrogels for articular cartilage repair.

2.2 Synthesis of methacrylated chitosan and gelatin

Synthesis of chitosan methacrylate (CHMA). CHMA was synthesized according to a previously reported method.[35] Briefly, 3 g of chitosan was dissolved in 300 mL of distilled water with the addition of 4 mL of acetic acid (around 1.33%). The chitosan solution was then heated to 60 °C, and 3 mL of methacrylic anhydride was introduced. No light avoidance was necessary during the reaction process, and the reaction proceeded for 4 hours under vigorous stirring. Upon the completion of the reaction, 10% (wt/vol) of sodium bicarbonate solution was slowly added until the pH reached a range of 5.8–6.2. Subsequently, the solution underwent dialysis against deionized water using a dialysis tube with a molecular weight cutoff weight of 8000–14 000 Da for 4 days. Finally, the pure product was obtained by lyophilization and characterized by ^{1}H nuclear magnetic resonance (^{1}H NMR) spectroscopy and Fourier transform infrared (FTIR) analysis.

Synthesis of gelatin methacrylate (GelMA). GelMA was synthesized according to a previously reported method.[36] Briefly, 100 g of gelatin was dissolved in 1000 mL of phosphate-buffered saline (PBS, 10 mM, pH 7.2 ± 0.2). The gelatin solution was then heated to 50 °C, and 20 mL of methacrylic anhydride was added. The reaction was allowed to proceed for 3 h under vigorous stirring. Subsequently, the solution underwent dialysis against deionized water at 40 °C using a dialysis tube with a molecular weight cutoff weight of 8000–14 000 Da for 4 days. Finally, the pure product was obtained by lyophilization.

2.3 Preparation of composite hydrogels

The composite hydrogels with various contents of CHMA were prepared using photo-initiated free radical co-polymerization.[37] Specifically, CHMA concentrations of 0.5 wt%, 1.0 wt%, and 1.5 wt% were used, while the GelMA concentration was fixed at 10 wt%. GelMA and CHMA mixtures were added into appropriate amounts of deionized water containing 0.05 wt% LAP photo-initiator to GC$_m$ hydrogel precursor solution by exposing them to a 405 nm curing light source (EFL-LS-1601-405, EFL, China) for 1 minute. The obtained hydrogels were designated as GC$_m$, where m represents the weight fractions of CHMA (m = 0.5, 1.0 and 1.5 respectively). The pure GelMA hydrogels served as the control group.

2.4 Rheological measurement

Rheological experiments were conducted using a rheometer (discovery HR-20, TA Instruments, USA) equipped with a 20 mm diameter parallel plate. All experiments were conducted at a

controlled temperature of 37 °C to simulate physiological conditions. A gap of 500 μm was maintained between the parallel plate and Peltier during the rheological measurements to ensure accurate and reproducible results. Amplitude sweep analysis was performed to assess the viscoelastic behavior of the precursors and hydrogels under varying strains from 0.1% to 1000%. The thermo-sensitivity of the hydrogels was measured by using an oscillatory temperature sweep ranging from 5 °C to 45 °C. The gelation kinetics of pure GelMA hydrogels and GC_m hydrogels were evaluated through dynamic oscillatory time sweeps using a quartz plate connected to a blue light source. Subsequently, a frequency sweep was conducted on the cross-linked hydrogels at a strain of 1.0%, covering a frequency range from 0.1 rad s^{-1} to 100 rad s^{-1}. The network structures of hydrogels were analyzed using the rubber elastic theory. The approximate relationship between polymer network pore size (V, m^3) and storage modulus (G, Pa) is as follows:

$$G \approx \frac{K_B T}{V}$$

where K_B stands for the Boltzmann constant (1.38×10^{-23} J K^{-1}), and T is the temperature (310.15 K).

2.5 Uniaxial compressive testing

Cylindrical hydrogel samples (diameter: 8 mm, height: 5 mm) underwent unconfined compressive testing using a universal testing machine (DCS-20S, Sasck China) with a crosshead speed of 5.0 mm min^{-1}. The compression limit was set at 90% strain to protect the load cell. The Young's modulus (E) was determined as the slope of the stress–strain curve at low strain (<15%).

2.6 Swelling behavior measurement of composite hydrogels

Cylindrical samples of GelMA and GC_m hydrogels, with a height of 5 mm and a diameter of 8 mm, were prepare using a custom-designed silicone mold as a template for the swelling test. The precursor materials were injected into the mold and subsequently photo-cured using 405 nm light irradiation at an intensity of 10 mW cm^{-2} for a duration of 1 minute to form the hydrogel network. The freshly formed hydrogels were initially weighed (W_i) and then completely immersed in 30 mL of PBS at room temperature for 24 hours. The weights (W_s) of the hydrogel samples were recorded at specific time points of 0.5, 1, 2, 4, 8, and 24 hours. The swelling ratio (SR) was defined as the ratio of the mass of the swollen hydrogel at the specified time to its initial mass. The calculation formula is as follows:

$$SR\ (\%) = W_s/W_i \times 100\%$$

where W_i represents the initial weight of the fresh formed hydrogels, and W_s corresponds to the weights of swollen hydrogels at pre-set time points.

2.7 Microstructure characterization

Microstructural characterization was conducted on GC_m composite hydrogels by scanning electron microscopy (SEM, Phenom Pharos G2, Netherlands) operating at an accelerating voltage of 4 kV. To prepare the hydrogel samples for SEM observation, the GelMA and GC_m hydrogels were initially lyophilized at −60 °C for 24 h to eliminate any residual water content. Subsequently, the lyophilized samples were fully immersed in liquid nitrogen and then fractured to expose their cross-sectional structures. Prior to SEM imaging, a thin layer of gold was sputter-coated onto the sample surfaces using an ion sputter current of 15 mA for 60 s.

2.8 *In vitro* degradation of hydrogels

The *in vitro* degradation test was conducted by immersing the hydrogel sample in 15 mL of PBS at 37 °C. The dried hydrogel samples were initially weighed and placed in the PBS solution. After 3, 5, 7, 14, 21, and 30 days, the samples were washed with distilled water, freeze-dried, and then reweighed. The degradation rate (W_L) was calculated by:

$$W_L\ (\%) = (W_a - W_d)/W_a \times 100\%$$

where W_a is the original weight of the dried hydrogel sample, and W_d is the weight of the dry sample at the predetermined time.

2.9 Embedded 3D printing of composite hydrogels

The hydrogel bioink was deposited onto cell culture dishes containing a κ-carrageenan sub-microgel suspension using a custom-designed micro-extrusion-based 3D bioprinter. For improved visualization during the printing process, rhodamine labeled GelMA combined with CHMA was employed. Printing was performed with a 250 μm inner diameter needle (25 G), and the bioink flow rate was set to 10 μL min^{-1}. The printing speed was set to 50 mm s^{-1}. A 3D grid construct sized 12 × 12 × 2 mm^3 and various complex shapes including femur, meniscus, and humerus were printed with a layer thickness of 150 μm. Digital models were generated using Rhino software or downloaded from the 3D database (**https://www.thingiverse.com**).

2.10 Extraction and culture of bone marrow-derived mesenchymal stem cells (BMSCs)

BMSCs were isolated and harvested from 5-week-old New Zealand rabbits according to previously reported protocols. 6 mL of bone marrow aspirate were layered over a Ficoll gradient and centrifuged at 2000 rpm for 20 min at room temperature. The cells were then seeded in Dulbecco's modified Eagle's medium (DMEM, Cat. CM-Rb007, Pricella USA) supplemented with 10% fetal bovine serum (FBS, Cat. C04001-500, Gibco, USA) and 1% penicillin/streptomycin (Cat. 15070063, Gibco, USA), and cultured at 37 °C with 5% CO_2. Non-adherent cells were removed by medium changes during the first 6 hours, and then the culture medium was replaced every other day. Passage one of the BMSCs was obtained by trypsinization with 0.25% trypsin when the cells reached 70–80% confluence. Trilineage differentiation was induced by culturing the BMSCs in specific induction media. The induced cells were evaluated using staining methods to analyze their differentiation into osteogenic, adipogenic, and chondrogenic lineages.

2.11 Adhesion and chondrogenic differentiation of BMSCs on the GC_m hydrogels

200 μL of the GC_m hydrogel precursor solution was added to a 48-well plate and exposed to 405 nm blue light for 1 minute. The three-passage BMSCs were seeded onto the sterile GC_m composite hydrogels at a density of 3×10^5 cells per mL. Subsequently, the cells were cultured for 1, 3 and 5 days, respectively. F-Actin and nuclei were stained using FITC-phalloidin (YP0059L, UElandy, China) and 4,6-diamidino-2-phenylindole (DAPI, Cat. C0065, Solarbio, China) to visualize the morphology and behavior of cells. Furthermore, the BMSCs were cultured with chondrogenic induction differentiation medium (PD-023, Pricella, China) for an additional 21 days. The differentiated cells were labeled with Collagen-Type-II (Cat. 28459-1-AP, 1:100, Proteintech, China) and aggrecan (Cat. DF7561, 1:100, Affinity, China). The nuclei were labeled with DAPI. Immunofluorescence images were obtained using a confocal laser scanning microscope (CLSM, Stellaris 5, Leica, Germany), and all images were analyzed and quantified with ImageJ software.

2.12 Quantitative real-time polymerase chain reaction (qRT-PCR)

For the BMSCs cultured on the surface of cross-linked GC_m composite hydrogels samples, cells were directly lysed on the surface of the gels before RNA extraction. The total RNA was extracted from the BMSCs and reverse transcribed into cDNA following standard experimental procedures. The relative transcript levels of Collagen-2a1, Sox9 and Aggrecan were detected by qRT-PCR (LightCycler 480 Instrument II PCR, Roche, Switzerland) with specific primers. GAPDH was used throughout as a housekeeping gene for normalization of fold-changes in gene expression. The primer sequences for genes are presented in Table 1.

2.13 3D Bioprinting of GC hydrogels loaded with BMSCs

BMSCs (10^7 cells per mL) were resuspended in the hydrogel precursor at 37 °C and subsequently injected into a 5 mL syringe. The syringes were mounted on the modified micro-extrusion-based 3D bioprinter. The printing model was generated in Rhino software. The hydrogel was printed in cell culture dishes (BeyoGold, China) already covered with κ-carrageenan. Micro-extrusion was executed utilizing a 250 μm inner diameter needle at a bioink flow rate of 10 μL min^{-1} and constructs with dimensions of $12 \times 12 \times 1$ mm^3 were then created using the suspension printing technique. The printing speed was set to 50 mm s^{-1}. After printing, scaffolds were exposed to 405 nm blue light. PBS was added to wash the κ-carrageenan bath. Finally, DMEM supplemented with 10% FBS and 1% penicillin/streptomycin was added to the scaffold and cultured at 37 °C with 5% CO_2.

2.14 Morphology and chondrogenic differentiation of BMSCs within the 3D bioprinted $GC_{1.0}$ hydrogels

The survival of BMSCs within printed hydrogel constructs was identified using a live/dead staining assay after culturing for 3 days. For the live/dead staining assay, the cells were incubated with calcein-AM/PI (Cat. C2015M, Beyotime, China) for 30 min and examined using a fluorescence microscope. Furthermore, F-actin and nuclei were stained using FITC-phalloidin and DAPI to visualize the morphology and behavior of the cells at 5 days. Simultaneously, the constructs were transformed into chondrogenic differentiation medium until day 27. Then the differentiated BMSCs were labeled with Collagen Type II (Cat. 28459-1-AP, 1:100, Proteintech, China) and Aggrecan (Cat. DF7561, 1:100, Affinity, China). The nuclei were labeled with DAPI. Immunofluorescence images were obtained by CLSM to observe whether the material could successfully induce the differentiation of BMSCs.

2.15 *In vitro* hemolysis test

The hemolysis ratio of GC_m hydrogels at different concentrations was tested *in vitro*. The sample was dissolved in saline and warmed to 37 °C. Subsequently, 60 μL of erythrocyte stock dispersion was added into the sample suspensions (3 mL) and incubated at 37 °C for 1 h. Afterwards, the mixtures were centrifuged at 1500 rpm for 5 min. The absorbance of the supernatant was measured at 545 nm using a UV-Vis spectrophotometer (UV-1100, Mapada, China). Saline and distilled water served as positive control and negative control, respectively. The hemolysis rate (HR) was calculated by:

$$\mathrm{HR}\ (\%) = \frac{D_t - D_{nt}}{D_{pt} - D_{nt}} \times 100\%$$

where D_t, D_{nt}, and D_{pt} were the absorbance of the sample, the saline, and distilled water, respectively.

2.16 *In vivo* biocompatibility and biodegradation evaluation

The ICR mice (male, 16–18 g) were purchased from Beijing Vital River Laboratory Animal Technology Co., Ltd and housed in a quarantine room at the laboratory animal center, Ningbo University, for at least one week. All animal procedures strictly adhered to the guidelines and were approved by the Institutional Animal Care and Use Committee of Ningbo University.

Table 1 Reverse transcription-quantitative polymerase chain reaction primer sequences

	Primer (5′ → 3′)	
Gene	Forward	Reverse
Collagen 2a1	GCAACAGCAGGTTCACTTACAC	AGGAAGGGCAAACGAGATGG
Sox9	CTGGAGACTGCTGAACGAGAG	TCCGCCTGCCCATTCTTC
Aggrecan	CAACGCATTGAGTGTGAGCATC	CAGCACCACCTCCTTGTCC
GAPDH	CCACTTTGTGAAGCTCATTTCCT	TCGTCCTCCTCTGGTGCTCT

For subcutaneous implantation, the mice were anesthetized with isoflurane. Subsequently, 150 μL of hydrogel precursor solution was subcutaneously injected into the back and solidified by blue light at 405 nm for 1 min. At 1, 3, and 7 days, mice were euthanized without pain, and the tissue samples with hydrogel implants were fixed in 4% paraformaldehyde fixative, dehydrated in ethanol, embedded in paraffin, deparaffinized, rehydrated, and subjected to immunohistochemical CD68 staining (GB113109, 1:200, Servicebio, China) to assess histocompatibility. In addition, painless euthanasia was performed on mice for degradation observation on days 7, 14, 21, and 28. The samples containing hydrogel implants was fixed in 4% paraformaldehyde fixative, dehydrated in ethanol, embedded in paraffin, deparaffinized, rehydrated, and then subjected to hematoxylin and eosin (H&E) staining for assessing the *in vivo* degradation. At predetermined time intervals, the hydrogels were removed from subcutaneous tissues and then dried at 37 °C. The weight of each sample was recorded for calculating the degradation ratio.

2.17 Surgical implantation and histological analysis

Nine skeletally mature New Zealand rabbits (5–6 months old) weighing 2.9–3.2 kg were used for cartilage repair *in vivo*. All animal procedures strictly adhered to the guidelines and were approved by the Institutional Animal Care and Use Committee of Ningbo University (ethical registration number: 11893). Following a one-week acclimation period, rabbits were anesthetized with 10% sodium pentobarbital (2.0–3.0 mL kg^{-1}, 0.8 mL min^{-1}) injection at the ear margin. Bilateral knee joints underwent patella incision after disinfection, and dissection continued until the articular cartilage was exposed. An osteochondral defect (3.5 mm in diameter, 4 mm in depth) was created using a surgical drill bit. Subsequently, the 3D bioprinted $GC_{1.0}$ hydrogel and BMSCs-laden $GC_{1.0}$ hydrogel were tightly implanted into the osteochondral defect of each joint separately. For the blank group, the defect on the lateral condyle of the other knee of the same rabbit was left empty. Each group contained five samples. Following implantation, the surgical incision was closed layer by layer, and intramuscular injections of penicillin (200 000 units) were administered daily for the initial 5 postoperative days.

The rabbits were provided with water and food, housed in separate cages, and allowed free movement. Sacrifice occurred at 6 weeks postoperatively by inhaling an excess of CO_2. After joint photography and micro-computerized tomography (Micro-CT), samples were fixed in 4% formalin, decalcified, embedded in paraffin, and sliced at a thickness of approximately 8 μm for H&E staining and safranin-O/fast green (SOG). A simple histological–histochemical cartilage scoring system was validated.[38] Samples, randomly selected, were assessed by two independent surgeons blinded to the treatment and time points. Four parameters were evaluated: nature of the predominant tissue, structural characteristics, freedom from degeneration changes in adjacent cartilage, and freedom from cellular changes in degeneration.

For the detection of Collagen type II expression, a rabbit monoclonal antibody against Type II Collagen (28459-1-AP, 1:100, Proteintech, China) was employed, followed by a horseradish peroxidase-conjugated anti-rabbit antibody (Cat# MBS571213 1:100, Dako, Denmark). Both antibodies were diluted in PBS and colorized with diaminobenzidine tetrahydrochloride (DAB, Cat. 7411-49-6 Yeasen, China). Morphological changes in slices were observed using a microscope and imaging analysis system. Quantitative analysis of Collagen type II was performed using ImageJ.

2.18 Statistical analyses

Statistical analyses were conducted using GraphPad PRISM software (GraphPad Software Inc., La Jolla, CA, USA, RRID: SCR_00298) and Origin software (OriginLab Corporation, Northampton, MA, USA), version 2021. The data were expressed as the mean ± SEM. For multiple group comparisons, one-way analysis of variance (ANOVA) or two-way ANOVA tests were applied, followed by a Tukey *post hoc* test. Statistical significance was determined at $*p < 0.05$, $**p < 0.01$, $***p < 0.005$, and $****p < 0.001$.

3 Results and discussion

3.1 Preparation, viscoelasticity, and microstructures of GC_m composite hydrogels

Cell-adhesion responsive hydrogel scaffolds were synthesized *via* a one-step photopolymerization of methacrylated gelatin (GelMA) and chitosan (CHMA). GelMA facilitated cell adhesion and CHMA was incorporated to stimulate cellular aggregation. The synthesis of GelMA and CHMA was achieved by bonding methacryloyl moieties to the molecular backbones of gelatin and chitosan. The chemical structures of GelMA and CHMA were analyzed using Fourier transform infrared (FTIR) and ^{1}H nuclear magnetic resonance (^{1}H-NMR) spectroscopy techniques. As shown in Fig. S1a (ESI†), a new characteristic peak at 880 cm^{-1} corresponding to the wagging vibrations of $-CH_2$ groups in the FTIR spectra of GelMA was observed, indicating successful integration of methacrylate moieties into the gelatin structure. Additionally, two new peaks at 5.7 and 5.9 ppm were evident in the ^{1}H-NMR spectra of GelMA (Fig. S1b, ESI†), further confirming the incorporation of vinyl groups into gelatin. The substitution degrees of 42.5% were determined for GelMA through quantitative analysis using ^{1}H-NMR spectroscopy. FTIR spectra of the chitosan and CHMA samples were presented in Fig. S1c (ESI†). Three new peaks contributed by the newly formed amide were observed at 1654 cm^{-1}, 1536 cm^{-1} and 1315 cm^{-1}, corresponding to the amide I band (C═O stretching), amide II band (N–H deformation and C–N stretching) and amide III band in the CHMA spectrum. Moreover, typical vinyl protons in CHMA showed chemical shift signals at 5.6–6.0 ppm (Fig. S1d, ESI†). The substitution degrees of CHMA were around 19.1%, according to ^{1}H-NMR measurements.

To optimize the polymer blend for use as an engineered cellular responsive hydrogel, CHMA concentrations of 0.5 wt%,

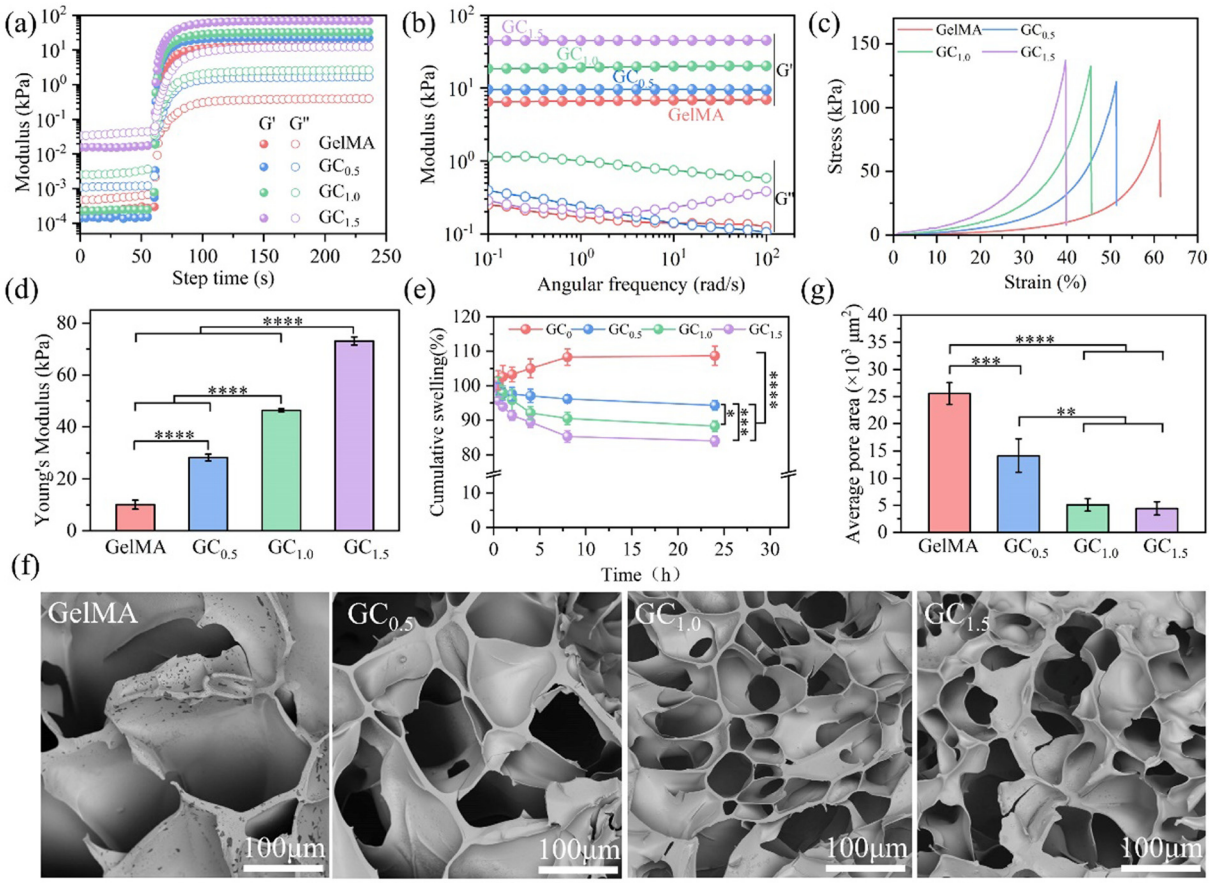

Fig. 1 Fig. 1 Characterization of GelMA and GC$_m$ hydrogels with different CHMA concentrations. (a) Time-sweep and (b) frequency-sweep rheological analyses of the GelMA and GC$_m$ hydrogels at 37 °C. (c) Compression stress–strain curves and (d) Young's modulus of the GelMA and GC$_m$ hydrogels. (e) Swelling behavior of the GelMA and GC$_m$ hydrogels within PBS. (f) SEM images and (g) average pore area of the freeze-dried GelMA and GC$_m$ hydrogels.

1.0 wt%, and 1.5 wt% were examined, while maintaining a fixed GelMA concentration of 10 wt%. The blend solution of GelMA and CHMA was exposed to 405 nm blue light with an intensity of 10 mW cm^{-2} in the presence of initiator LAP, resulting in the formation of elastic hydrogels. These hydrogels were denoted as GC$_m$, where G represents GelMA, C signifies CHMA, and m corresponds to the respective CHMA percentage (m = 0.5, 1.0, and 1.5). To assess the impact of varying CHMA concentrations on the kinetics of gelation and the resultant viscoelastic properties, the evolution of the storage modulus (G') and loss modulus (G'') was continuously monitored during photo-irradiation. As shown in Fig. 1a, the GC$_m$ mixtures exhibited typical characteristics of a liquid state prior to photo-crosslinking. Upon photo-irradiation, G' rapidly increased and surpassed G'' within 8 s for all examined samples, indicating an efficient transition to a gel state. Subsequently, both G' and G'' continued to rise steadily until reaching a stable plateau, which indicated the formation of a fully established covalent crosslinked network. Moreover, the concentration of CHMA had a pivotal influence on the mechanical stability of the hydrogels. Higher concentrations of CHMA resulted in higher G' values. Specifically, the G' values were approximately 12.66, 22.12, 32.59, and 70.22 kPa for GelMA alone and CHMA concentrations of 0.5 wt%, 1.0 wt%, and 1.5 wt%, respectively. Moreover, these G' values almost remained constant across the frequency range from 0.1 to 100 rad s^{-1}, indicating the stability of the network structures of the GC$_m$ hydrogels (Fig. 1b). Additionally, amplitude sweeps showed that nonlinear strain values surpassed 100% across all precursors and hydrogel formulations (Fig. S2, ESI†), indicating robust physical interactions between GelMA and CHMA, as well as the formation of stable linkages after covalent crosslinking. These mechanically stable networks are essential for the hydrogels to provide sufficient support for the growth of stem cells and promote chondrogenic differentiation, as indicated by previous studies.[39,40]

The mechanical properties of the GC$_m$ hydrogels with varying CHMA concentrations were further evaluated using uniaxial compressive testing. The compressive stress–strain curves for these hydrogels are shown in Fig. 1c and Fig. S3 (ESI†). Both the individual GelMA and CHMA hydrogels showed a moderate compressive resilience, with a peak strength of 90.2 kPa and 80.7 kPa at respective compressive strain thresholds of 61% and 43%. A notable enhancement in the ultimate compressive strength was observed when the CHMA concentration in the GC$_m$ hydrogels increased from 0.5 wt% to 1.0 wt% and 1.5 wt%, reaching values of 120.2 kPa, 133.32 kPa, and 136.8 kPa,

respectively. Correspondingly, the Young's modulus increased from 10.1 kPa of GelMA to 28.3 kPa, 46.4 kPa and 73.1 kPa for $GC_{0.5}$, $GC_{1.0}$, and $GC_{1.5}$, respectively (Fig. 1d). These improvements in mechanical properties of the composite hydrogels were mainly attributed to the enhanced covalent interactions between GelMA and CHMA.

Hydrogels intended for tissue repair should possess controllable swelling properties to avoid excessive swelling or deswelling in physiological fluids. The swelling ratios were determined by comparing the weights of the hydrogels before and after immersing in phosphate-buffered saline (PBS) at 37 °C for a duration of 24 hours (Fig. 1e). The equilibrium swelling ratio of the GelMA hydrogel was 109.5%, while the hydrogels with incorporated CHMA at concentrations of 0.5 wt%, 1.0 wt%, and 1.5 wt% exhibited decreased swelling ratios of 94.8%, 87.5%, and 82.0%, respectively, indicating that an increase in CHMA content correlates with a decline in swelling ratio. The observed swelling behavior is attributed to the pH-responsive and porously crosslinked architecture, which was further characterized by the microporous density and dimensions within the hydrogels. Scanning electron microscopy (SEM) analyses revealed that, following lyophilization, all hydrogels maintained a characteristic three-dimensional porous structure (Fig. 1f). Notably, the CHMA concentration had a pronounced effect on the microporous size distribution. As the CHMA concentration increased from 0.5 wt% to 1.0 wt% and 1.5 wt%, the corresponding pore area decreased progressively from 14.4×10^3 to 5.1×10^3 and 4.4×10^3 μm^2, which were all smaller than 25.6×10^3 μm^2 of GelMA hydrogels (Fig. 1g). Additionally, the rubber elastic theory was employed to elucidate the microstructural characteristics of the hydrogels, revealing the presence of nanostructures within the GC_m hydrogels (Table S1, ESI†). These results further demonstrated the formation of a densely crosslinked structure at higher CHMA concentrations. Furthermore, the *in vitro* degradation profiles of all hydrogels were quantified by monitoring the mass loss in PBS at 37 °C (Fig. S4, ESI†). The GelMA hydrogels displayed a progressive loss of structural integrity, undergoing complete degradation by the 21st day. In contrast, the GC_m hydrogels showed reduced degradation rates, thereby maintaining their structural integrity for an extended timeframe. By the 30th day, the remaining mass of the $GC_{0.5}$, $GC_{1.0}$, and $GC_{1.5}$ hydrogels was 17.0%, 34.5%, and 45.7%, respectively, suggesting that the GC_m hydrogels could provide sustained support conducive to cellular proliferation and tissue regenerative processes.

3.2 Biomimetic printing using GC hydrogels

Due to the inherent thermos-responsive sol–gel transition ability, GelMA and its composite hydrogels have been attractive materials for 3D bioprinting applications mimicking the native tissues and organs.[41] However, the utilization of thermosensitive bioinks for direct 3D bioprinting presents notable challenges, predominantly in preserving the structural fidelity of intricate constructs during the phase transition from a heated liquid state to a cooled gel state. To address these challenges, we employed a κ-carrageenan sub-microgel suspension printing approach for the freedom printing of GC_m composites based on our recent reports.[39] The κ-carrageenan sub-microgel suspension serves as a supportive matrix, ensuring the retention of the printed structure's geometry during printing and mitigating the rapid sol–gel transition (Fig. 2a). Post-printing, the κ-carrageenan sub-microgels can be readily eliminated *via* successive PBS washes. Micro-extrusion was executed utilizing a 250 μm inner diameter needle at a bioink flow rate of 10 μL min^{-1}. For enhanced visualization, rhodamine-labeled GelMA was composited with CHMA and then printed in the κ-carrageenan medium.

As shown in Fig. 2b, a large-scale 3D grid construct (designed size: $12 \times 12 \times 2$ mm^3) with a 150 μm layer thickness was successfully printed by using $GC_{1.0}$ as an illustrative example. The grid showcased exceptional structural integrity, with individual filament widths of approximately 160 μm and inter-filament spacing of about 300 μm, as verified by confocal laser scanning microscopy (Fig. 2c). A diminished filament diameter, achieved through the employment of a larger diameter printing nozzle, was mainly attributed to an interplay of rapid printing velocity, a reduced flow rate of bioink, and the reversible thermosensitivity characteristic of the $GC_{1.0}$ bioink (Fig. S5, ESI†). Furthermore, the 3D construct presented an interconnect network (Fig. 2d), which is crucial for facilitating cellular growth within the scaffolds. Various complex shapes including femur, meniscus, and humerus are further replicated by using $GC_{1.0}$ inks (Fig. 2e–g). The printed femur faithfully captured its intricate details, such as the head, neck, and shaft, providing a faithful representation of this crucial bone in the human body (Fig. 2e). Similarly, the printed meniscus showcased its unique inner "C" shape and outer "O" shape, accurately mimicking the fibrocartilaginous structure (Fig. 2f). Additionally, the printed humerus exhibits the characteristic features of this long bone, including the head, greater and lesser tubercles, and the shaft (Fig. 2g). These results demonstrated that the printability of GC_m hydrogels for accurately replicating biomimetic shapes and structures.

3.3 Guiding BMSC micro-aggregate growth to enhance chondrogenesis on GC_m hydrogel matrices

The designed GC_m hydrogels provided a biochemical and mechanical micro-environment for cell adhesion, growth, and differentiation. To evaluate the potential of GC_m scaffolds in guiding the intercellular aggregation, bone marrow-derived mesenchymal stem cells (BMSCs) were employed and initially cultured on two-dimensional (2D) scaffolds. The pluripotency of BMSCs was confirmed by successful differentiation into osteoblasts, chondrocytes, and adipocytes (Fig. S6, ESI†). The adhesion and growth behaviors of BMSCs seeded on GC_m hydrogels with CHMA concentrations of 0.5 wt%, 1.0 wt% and 1.5 wt% were visualized using CLSM after staining with FITC-phalloidin and DAPI. As shown in Fig. 3a and Fig. S7 (ESI†), the CHMA concentrations profoundly impacted the morphology of cell adhesion. The BMSCs on the GelMA hydrogels exhibited a typical spreading morphology, while those on the GC_m hydrogels primarily formed multi-cellular aggregates.

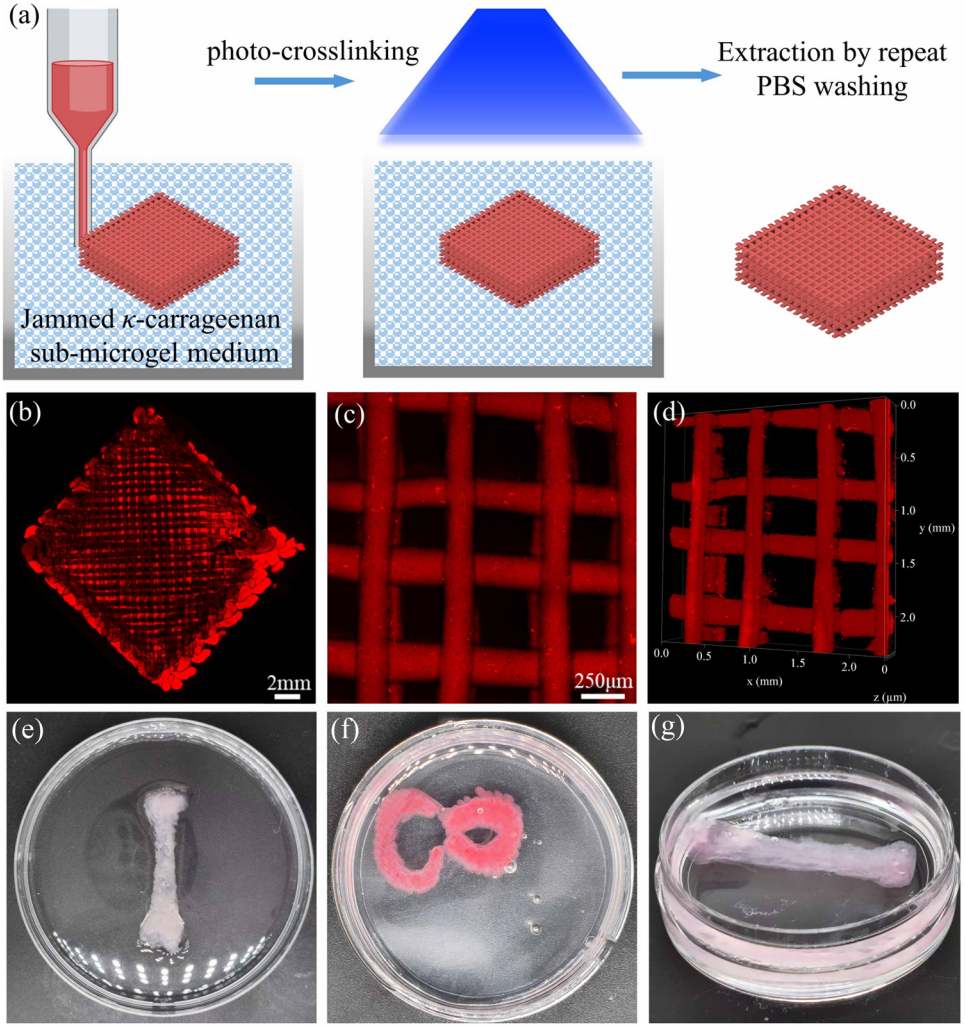

Fig. 2 3D bioprinting biomimetic scaffolds using GC hydrogels within a jammed κ-carrageenan suspension bath. (a) Schematic illustration of 3D embedded bioprinting processes by using a κ-carrageenan suspension bath. (b)–(d) CLSM images of a 3D printed high-resolution grid construct, including the perspectives of full-scale image (b), projection (c) and 3D reconstruction (d). (e)–(g) Images of 3D printed femur (e), meniscus (f), and humerus (g) shapes using the $GC_{1.0}$ hydrogel.

Additionally, the number of cells on the GelMA matrix on the third day was higher than on the first and fifth days, but the cell size was the smallest, indicating highly active cell proliferation on the third day. In contrast, from the first day to the third and fifth days, the cells not only increased in size but also significantly increased in aggregate number on the GC hydrogel, further demonstrating the delicate regulatory role of the GC hydrogel in cell adhesion, proliferation, and aggregation. The BMSCs on $GC_{1.0}$ hydrogels showed the largest aggregation compared to $GC_{0.5}$ and $GC_{1.5}$. This could be attributed to the lower CHMA concentration being more favorable for cell adhesion and spreading, while the higher CHMA concentration had an inhibitory effect. It is worth noting that these aggregates consisted of plenty of low-spreading cells, which is different from previous reports[42,43] and suggests the synergistic effects of GelMA and CHMA on cell adhesion and aggregation. Furthermore, the BMSCs exhibited significant proliferation and aggregation within 5 days, indicating the high bioactivity of the GC_m hydrogels for BMSC growth.

The formation ratio of multicellular aggregates, the number of cells within a single aggregate, and the adhesion area of each aggregate were quantified based on the nucleus stained with DAPI and the cytoskeleton stained with FITC-phalloidin. After one day of culture, the average ratios of BMSC aggregates on the $GC_{0.5}$, $GC_{1.0}$, and $GC_{1.0}$ hydrogels were 36.5 ± 6.8%, 48.3 ± 3.8% and 48.6 ± 2.1% (Fig. 3b). Following 3 and 5 days of culture, the aggregation ratios significantly increased, excessing 50% and 75%. Specifically, the largest ratios of aggregates on the $GC_{1.0}$ hydrogel reached 88.5 ± 1.9% and 93.5 ± 1.7% at 3 and 5 days, respectively. These multicellular aggregates contained an average of 8.0 ± 1.7, 28.0 ± 4.04 and 12.7 ± 1.45 cells on the $GC_{0.5}$, $GC_{1.0}$, and $GC_{1.0}$ hydrogels on day 1, respectively (Fig. 3c). Following 3 and 5 days of culture, the corresponding cell numbers increased to 12.3 ± 0.9, 136 ± 17.1 and 24.3 ± 1.8, 24.7 ± 2.6, 239 ± 22 and 75.3 ± 6.9, respectively. Meanwhile, the average adhesion area of single aggregate on the $GC_{0.5}$, $GC_{1.0}$, and $GC_{1.5}$ hydrogels grow from about 5683 ± 437.4,

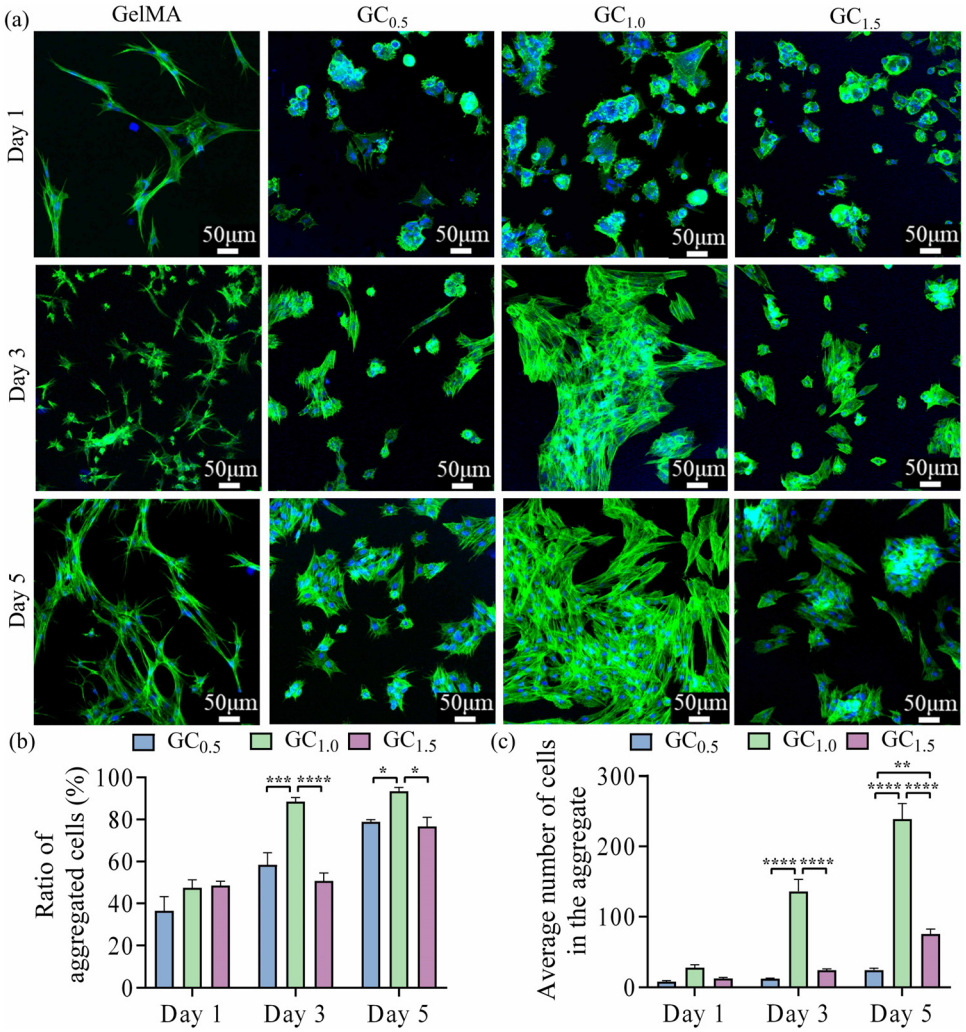

Fig. 3 Adhesion and aggregation behaviors of BMSCs on hydrogels. (a) Fluorescence microscopy images of BMSCs cultured on the GelMA and GC_m hydrogels (FITC-phalloidin for cytoskeleton, DAPI for nucleus) at 1, 3 and 5 days, respectively. (b) and (c) Percentage of the formed cell aggregates (b) and the average cell number within a single aggregate (c) counted by the stained cellular nuclei on day 1, 3 and 5. *$p < 0.05$, **$p < 0.01$, ***$p < 0.005$, and ****$p < 0.001$.

9694 ± 993.6 and 6033 ± 530.8 μm^2 to 6326 ± 1397, 44 752 ± 12 018 and 9261 ± 2454 μm^2, and 7175 ± 1424, 263 013 ± 71 361 and 24 017 ± 3101 μm^2, respectively, from day 1 to 3 and 5 (Fig. S8, ESI†). These results demonstrated that the GC_m hydrogel scaffolds possess a distinctive cellular-responsive nature that effectively regulates the formation of BMSC spheroids. In particular, the $GC_{1.0}$ hydrogel exhibited the most significant responsiveness to cell adhesion and aggregation. Previous studies have indicated that chitosan and its composite materials could influence calcium ion signaling, potentially facilitating the fusion of MSCs into spheroids,[44] which is crucial for chondrogenesis and cartilage regeneration. Additionally, the GC_m hydrogels, characterized by their elevated stiffness ranging from 28.3 to 73.1 kPa (as depicted in Fig. 1d), provided an optimal mechanical microenvironment conducive to the proliferation of cell spheroids. Hence, the integrated biochemical and biophysical properties of the GC_m hydrogels synergistically enhance the adhesion and aggregation of stem cells.

To evaluate the differentiation potential of BMSCs cultured on GC_m composite hydrogels into chondrocytes, immunofluorescence staining analysis was performed for Collagen II and Aggrecan (key markers of chondrocytes) after 21 days of incubation. The immunofluorescence images clearly showed the presence of Aggrecan and Collagen type II within differentiated BMSCs (Fig. 4a). Notably, the $GC_{1.0}$ group exhibited the highest fluorescence intensity for both Aggrecan and Collagen II compared to the other experimental groups and GelMA alone. The fluorescence intensities of Aggrecan and Collagen II expression on hydrogels were further quantitatively analyzed. The measured intensities for Aggrecan and Collagen II on $GC_{0.5}$, $GC_{1.0}$, and $GC_{1.5}$ hydrogels were 85.2 ± 5.7 and 93.3 ± 1.7, 124 ± 3.8 and 132.8 ± 16.9, and 110.3 ± 4.5 and 92.1 ± 2.1, respectively (Fig. S9, ESI†). These results suggested that the $GC_{1.0}$ hydrogel matrix promotes the synthesis and secretion of these cartilage-specific proteins.

Furthermore, gene expression analysis was performed to validate the immunofluorescence staining. The expression levels of Sox9, Collagen-2a1, and Aggrecan genes were measured *via* qRT-PCR experiment. Sox9 serves as an early chondrogenic marker, facilitating the synthesis of Aggrecan and Collagen type II.

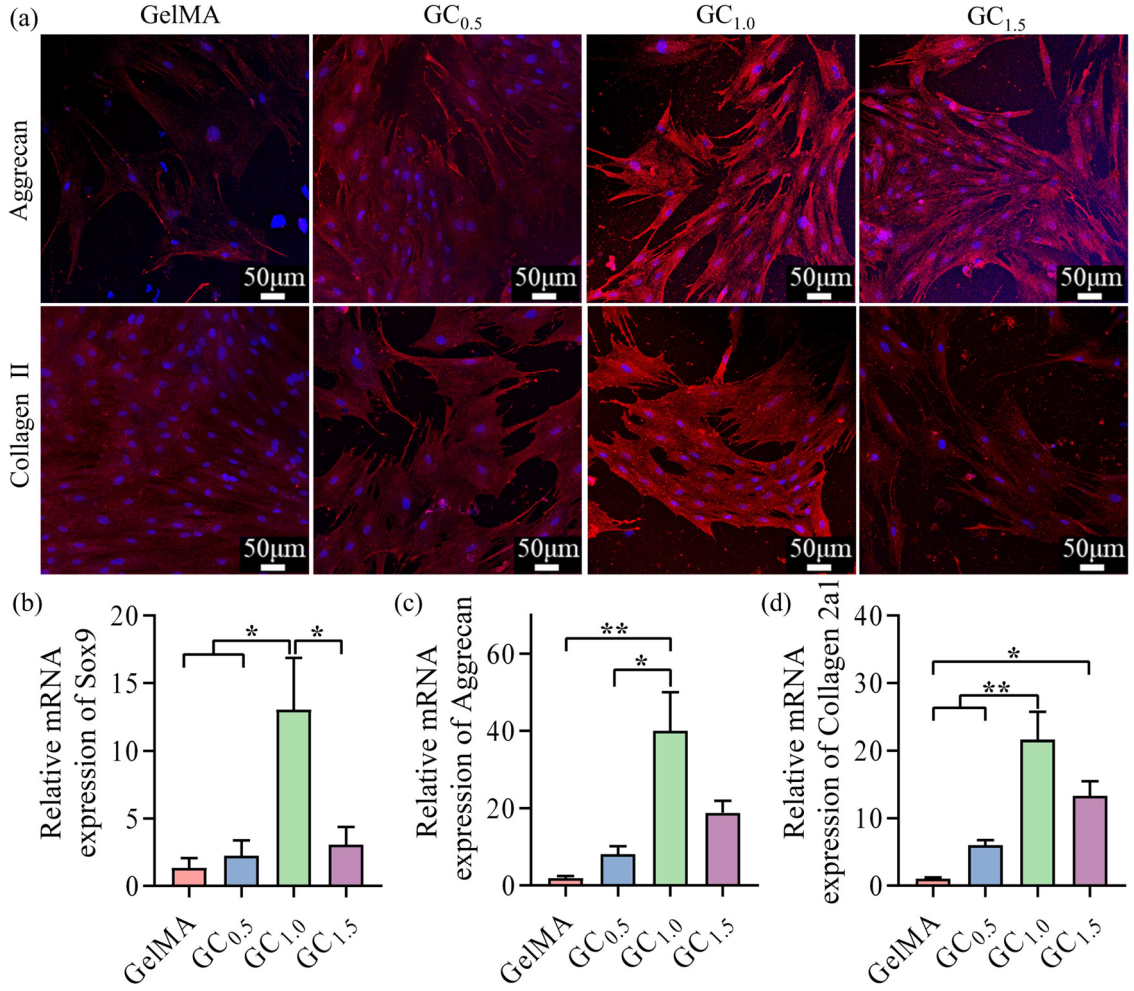

Fig. 4 Characterization of chondrogenic differentiation of BMSCs on hydrogels. (a) Immunofluorescence staining images of Aggrecan and Collagen-II protein expression. (b)–(d) Relative mRNA expression of Sox9 (b), aggrecan (c) and Collagen-2a1 (d). *$p < 0.05$, ** $p < 0.01$.

The Collagen 2a1 gene encodes Collagen type II. As shown in Fig. 4b–d, the gene expression of Sox9, Aggrecan and Collagen 2a1 in the GC_m groups showed a higher magnitude compared to the GelMA group. Particularly, the $GC_{1.0}$ group exhibited the most substantial upregulation of these genes among all the experimental samples, which was consistent with the immunofluorescence staining results. Consequently, the increased gene expression in the $GC_{1.0}$ group translated into higher protein production, indicating the effectiveness of the $GC_{1.0}$ hydrogel matrix in promoting chondrogenesis. These findings highlight the potential of the $GC_{1.0}$ hydrogel matrix as a promising tissue-engineering scaffold for promoting cartilage regeneration and repair.

3.4 BMSC-laden bioprinting and chondrogenesis within $GC_{1.0}$ hydrogels

Compared to cellular growth and differentiation on the hydrogel surface, the survival and aggregation of cells within 3D hydrogels pose challenges due to the restrictive nature of stiff and dense networks, which limit cellular movement and contact. However, stiff GC hydrogels may promote cell aggregation once degradation occurs. In order to investigate cellular behaviors within hydrogels, BMSCs at a density of 1×10^7 cells per mL were uniformly distributed into $GC_{1.0}$ precursor, and constructs with dimensions of $12 \times 12 \times 1$ mm^3 were then created using the suspension printing technique. These bioengineered hydrogel constructs showed long-term stability, which is important for cell growth and chondrogenic differentiation (Fig. 5a).

The viability of BMSCs within the bioprinted hydrogels was initially assessed using a standard live/dead assay. The resulting live (green)/dead (red) images revealed that BMSCs within the $GC_{1.0}$ constructs exhibited isolated growth distribution on the initial day of cell culture (Fig. 5b). The cell survival rate reached 91.1%, robustly confirming the excellent safety of the $GC_{1.0}$ hydrogels, suspension bioprinting process and the subsequent photo-crosslinking procedure (Fig. S10, ESI†). To further examine the cell morphology of the $GC_{1.0}$ constructs, FITC-phalloidin (red)/DAPI (blue) staining images were captured after 5 days of cell culture. As shown in Fig. 5c, the BMSCs predominantly maintained a non-spreading morphology by day 5. Importantly, the connection with adjacent cells had already been established within the hydrogel networks, resembling the results

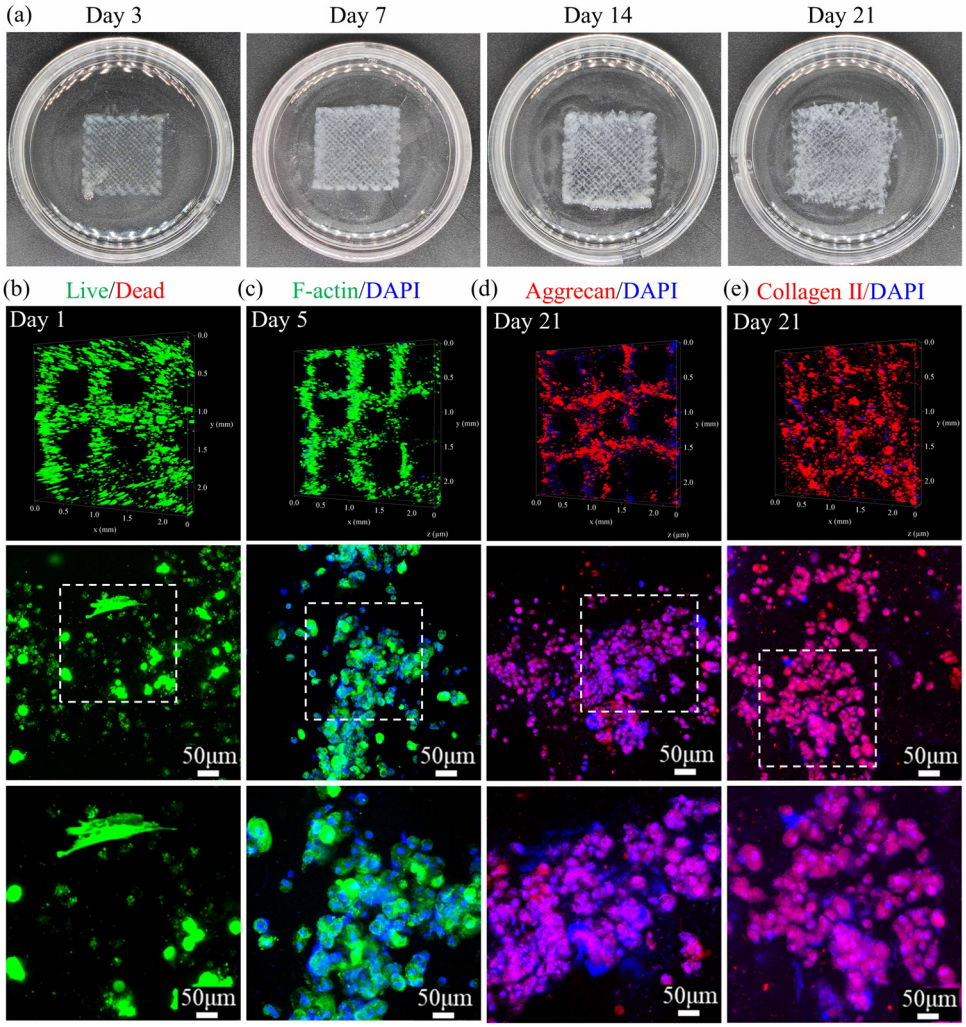

Fig. 5 BMSC-laden hydrogel bioprinting and chondrogenic differentiation. (a) Live (green)/dead (red) fluorescence images of BMSCs within bioprinted $GC_{1.0}$ scaffolds after 3 days of culture. (c) CLSM images of BMSCs within bioprinted $GC_{1.0}$ hydrogel scaffolds (FITC-phalloidin for cytoskeleton, DAPI for nucleus) on day 5. (d) and (e) Immunofluorescence staining images of aggrecan (d) and Collagen II expression after 21 days of culture (e).

seen in BMSC culture on the hydrogel surface. These results indicated that the $GC_{1.0}$ hydrogel provided a biodegradable and biochemical microenvironment for cell growth and interaction. We further analyzed the chondrogenic differentiation of BMSCs within the bioprinted hydrogels *in vitro* using Collagen II and Aggrecan immunofluorescence staining. As shown in Fig. 5d and e, BMSCs within the $GC_{1.0}$ hydrogel constructs maintained aggregate growth and exhibited positive staining for Collagen II and Aggrecan at 21 days, indicating their chondrogenic differentiation. These results further affirmed that $GC_{1.0}$ composite hydrogels have significant potential as a scaffold for augmenting the chondrogenic differentiation of BMSCs.

3.5 Biocompatibility and biodegradation properties of the $GC_{1.0}$ hydrogel

Potential biocompatibility and biodegradability are significant concerns in clinical applications. To address these concerns, the blood compatibility of the hydrogels was initially evaluated through a hemolysis test. Hemolysis, the release of hemoglobin resulting from the rupture of erythrocyte cell membranes in an incompatible environment, is a critical factor to assess hemocompatibility. According to ISO10993-4 standards for clinical hemostatic materials, the hemolytic ratio should be below 5%.[45] It was observed that the supernatant treated by the hydrogels exhibited a clear color, indicating their minimal hemolysis (Fig. 6a). The hemolysis ratios for the GelMA, $GC_{0.5}$, $GC_{1.0}$, and $GC_{1.5}$ hydrogels were 0.65%, 0.75%, 0.77%, and 0.79%, respectively, all lower than 5% (Fig. 6b). These results demonstrated the excellent hemocompatibility of GC_m composite hydrogels in accordance with ISO10993-4 standards.

The *in vivo* biocompatibility of the hydrogel underwent further assessment through subcutaneous implantation in mice. Following the subcutaneous implantation of the $GC_{1.0}$ hydrogel, the early inflammatory response was scrutinized at various time points (1, 3 and 7 days) using immunohistochemical staining with the macrophage antibody CD68 (Fig. 6c and d). The control group, without hydrogel implantation, served as a baseline of comparison. One day after implantation, a distinct

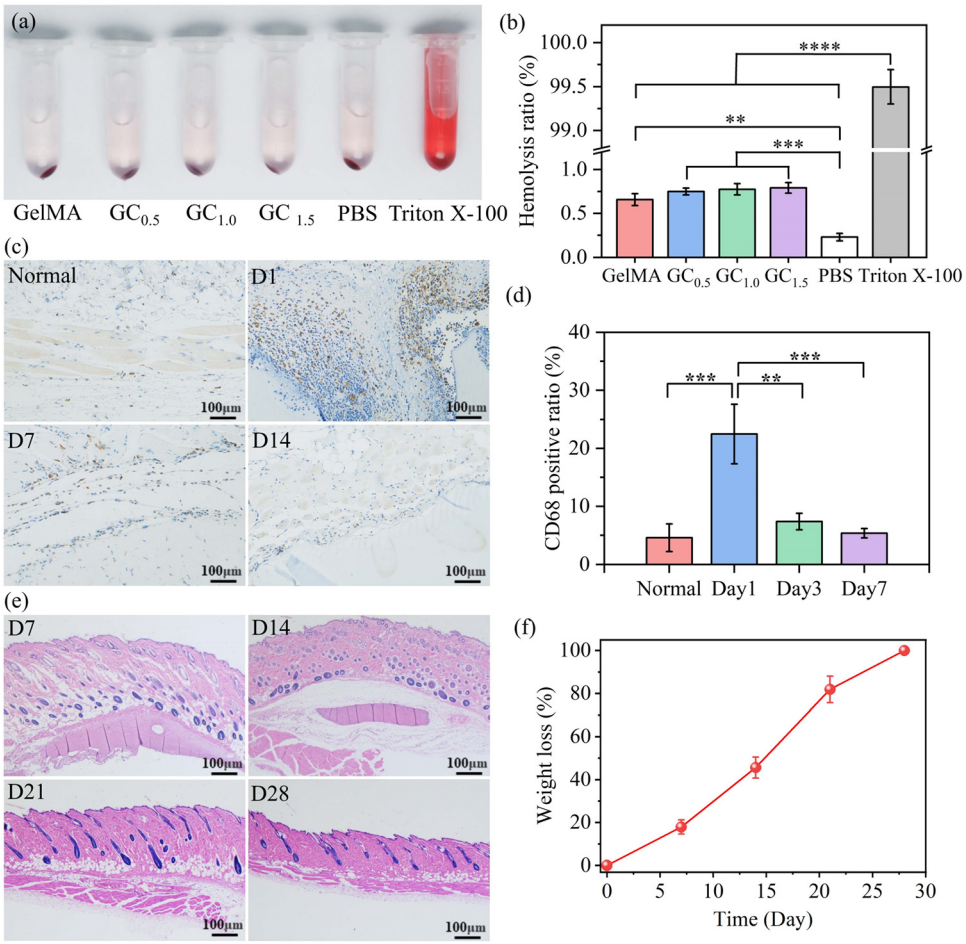

Fig. 6 Biocompatibility and biodegradation of hydrogels *in vivo*. (a) Hemolysis photos and (b) hemolysis rate of GelMA, $GC_{0.5}$, $GC_{1.0}$, $GC_{1.5}$, negative control (PBS) and positive control (0.1% Triton X-100). ***$p < 0.005$. (c) The immunohistochemical staining of CD68 expression in the surrounding tissues of $GC_{1.0}$ hydrogels after implantation for 1, 3, and 7 days, along with a control group. (d) Percentage of CD68-positive cells. ** $p < 0.01$. (e) H&E staining of the hydrogels after subcutaneous implantation on day 7, 14, 21 and 28. (f) Quantification of degradation ratio.

inflammatory response emerged. The hydrogel and subcutaneous tissue exhibited a significant presence of macrophages, evidenced by intense cytoplasmic staining, indicating an active inflammatory reaction triggered by the hydrogel implantation. Moreover, a substantial accumulation of macrophages occurred at the interface between the hydrogel and the surrounding tissue. As the implantation period progressed, changes in the inflammatory response were evident. Three days after implantation, there was a noticeable reduction in the number of macrophages in the tissue surrounding the hydrogel, signifying a gradual mitigation of the inflammatory reaction. By the 7th day, the inflammatory response had largely subsided, with minimal macrophage presence in the hydrogel vicinity. This suggests that the hydrogel had become well-tolerated by the surrounding tissue, evidenced by the absence of significant inflammation. These results indicated a favorable *in vivo* compatibility of the $GC_{1.0}$ composite hydrogels.

The synchronization of hydrogel degradation rate and new tissue growth rate is pivotal for successful tissue repair and regeneration. In the case of acute cartilage defects, the hydrogel degradation and the new tissue formation typically span a period of 4–8 weeks. The degradation rate of the $GC_{1.0}$ hydrogel was monitored over several weeks. As shown in Fig. 6e, the $GC_{1.0}$ hydrogels gradually degraded and eventually disappeared within the body after 28 days. Within the first week, the hydrogel exhibited a weight decrease of 17.9% (Fig. 6f), signaling a gradual erosion and breakdown process. By the end of the second week, a significant weight loss of 45.6% indicated an accelerated degradation process within the hydrogel structure. After three weeks, a substantial reduction in hydrogel mass, amounting to 81.9% of the initial mass, demonstrated continuous degradation through the erosion process, significantly decreasing the overall mass. These results highlighted the biodegradable nature of the $GC_{1.0}$ hydrogels, showcasing their potential for applications in tissue repair and regeneration. The controlled degradation rate of the hydrogel plays a vital role in providing an appropriate environment for cell migration, proliferation, maturation, and the organization of the extracellular matrix essential for effective tissue healing.

3.6 Bioprinted BMSC-laden $GC_{1.0}$ hydrogels for cartilage repair

The optimal $GC_{1.0}$ hydrogel, characterized by its ability to facilitate cell adhesion, aggregation, proliferation, and chondrogenic

differentiation while being biodegradable and biocompatible, shows promise for the repair of cartilage wounds. To assess its potential, we created articular cartilage defects in New Zealand rabbits, generating defects measuring 3.5 mm in diameter and 4 mm in depth within the patellar groove of femoral knee joints. Subsequently, bioprinted BMSC-laden $GC_{1.0}$ hydrogels with 3.6 mm diameter and 4 mm height were tightly implanted into the injury site, with printed $GC_{1.0}$ hydrogels without cells and PBS serving as the control and blank groups. After a 6-week post-implantation period, joint specimens were collected and thoroughly examined at the repair site to evaluate the repair efficacy. Remarkably, the $GC_{1.0}$ + BMSCs group exhibited extensive tissue regeneration, characterized by tissues mostly covered by a glossy and smooth membrane, while the $GC_{1.0}$ group showed partial repair of the defects, and defects persisted in the blank group (Fig. 7a). Micro-CT analysis further confirmed notable tissue repair, demonstrating clear evidence of newly formed tissues structurally similar to the surrounding tissue in the $GC_{1.0}$ + BMSCs hydrogel group (Fig. 7b). Additionally, the $GC_{1.0}$ + BMSCs group showed enhanced tissue repair and integration, with visibly improved macroscopic appearance and a more well-defined integration border zone. We further quantified the new cartilage formation in the defect area using International Cartilage Repair Society (ICRS) scores (Table S2, ESI†), a crucial indicator for comprehensive cartilage repair evaluation. Statistical analysis revealed significantly higher total ICRS scores in the $GC_{1.0}$ + BMSCs group compared to the control group (Fig. 7c–f). Specifically, the $GC_{1.0}$ + BMSCs group exhibited significantly higher total ICRS scores (9.2 ± 1.3) compared to both the $GC_{1.0}$ hydrogel (7.4 ± 0.55) and blank groups (3.0 ± 1.0). Detailed

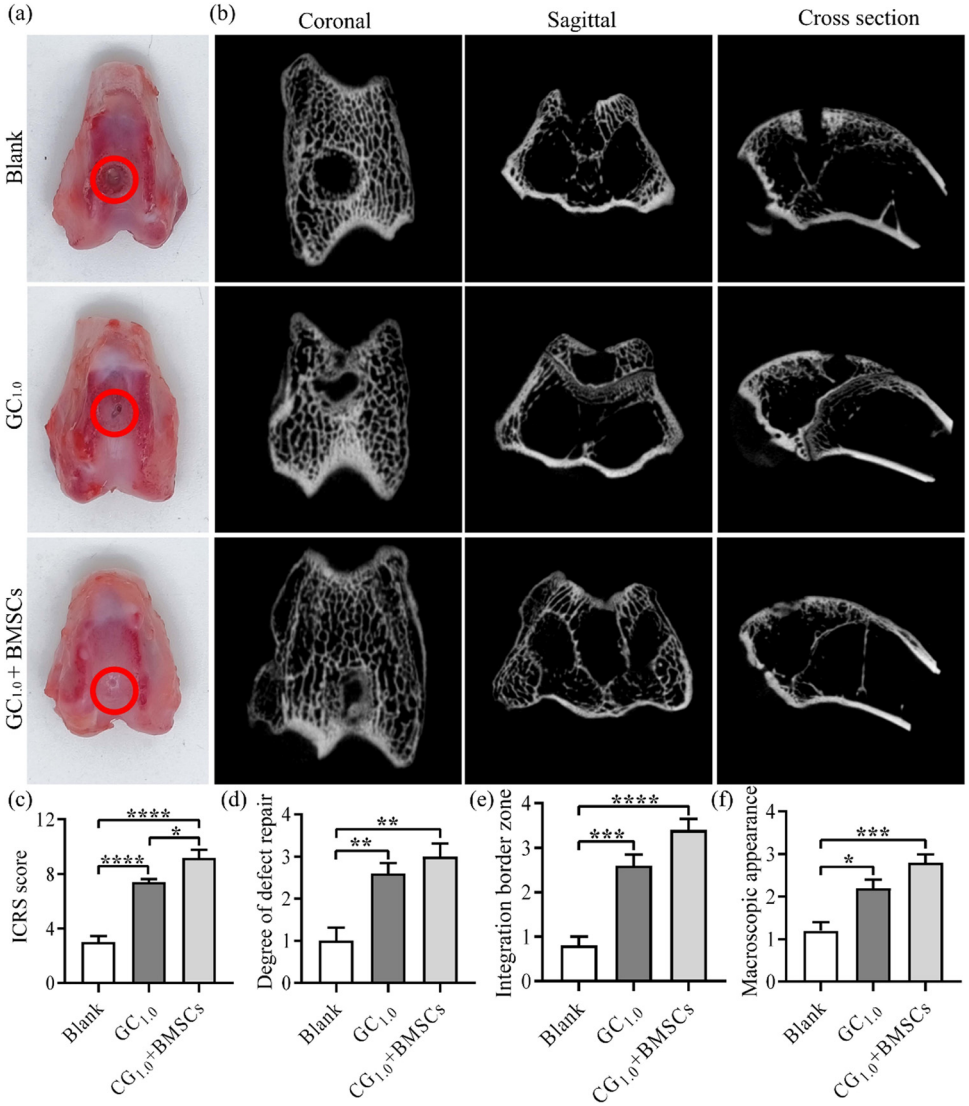

Fig. 7 Cartilage defect repair augmented with hydrogels embedded with BMSCs. (a) Macroscopic observation of cartilage defect repair. (b) Micro-CT observation of osteochondral defect repair using $GC_{1.0}$ and $GC_{1.0}$ + BMSC hydrogel scaffolds at 6 weeks. (c)–(f) The total ICRS scores (c), and degree of defect repair (d), integration border zone (e), and macroscopic appearance (f) for blank, $GC_{1.0}$ and $GC_{1.0}$ + BMSCs hydrogel scaffolds groups after 6 weeks of surgery. *$p < 0.05$, **$p < 0.01$, ***$p < 0.005$ and ****$p < 0.001$.

scoring of defect repair (3.0 ± 0.71), integration border zone (3.4 ± 0.55), and macroscopic appearance (2.8 ± 0.45) further demonstrated substantial improvement in the $GC_{1.0}$ + BMSCs hydrogel group. Overall, these results indicated superior recovery of cartilage in the $GC_{1.0}$ + BMSCs hydrogel group compared to the control groups six weeks post-implantation, highlighting the effectiveness of the $GC_{1.0}$ + BMSCs hydrogel in promoting cartilage repair and regeneration.

To comprehensively investigate the contribution of $GC_{1.0}$ and $GC_{1.0}$ + BMSCs hydrogels to cartilage-like tissue formation, tissues from the cartilage defect sites were analyzed through H&E staining, safranin-O/fast green (SOG) staining, and immunohistochemistry (IHC) staining for Collagen-II. As shown in Fig. 8a, H&E staining confirmed a notable increase in cartilage-like tissue formation with $GC_{1.0}$ + BMSC hydrogels compared to the other groups, corroborating micro-CT findings. Moreover, SOG staining demonstrated significant improvements in cartilage matrix deposition and organization in the $GC_{1.0}$ + BMSCs hydrogel group. In the $GC_{1.0}$ group, SOG staining revealed partial repair of the cartilage defects, evidenced by a moderate increase in cartilage matrix deposition compared to the blank group. In contrast, the blank group exhibited complete disorganization and severe reductions in SOG staining, indicating compromised cartilage integrity and matrix composition. IHC staining for Collagen-Type-II further supported the enhanced cartilage-like tissue formation in the presence of BMSC-loaded $GC_{1.0}$ hydrogels. Positive staining for Collagen-II was more pronounced and widespread in the $GC_{1.0}$ + BMSCs hydrogel group compared to the control group. Additionally, the O'Driscoll score, a semiquantitative assessment ranging from 0 to 24, was employed to evaluate cellular and tissue parameters (Table S3, ESI†). The total score of the $GC_{1.0}$ + BMSCs hydrogel group was found to be 16.6 ± 2.6, surpassing those of the $GC_{1.0}$ group (11.8 ± 2.68) and blank group (5.0 ± 2.0) (Fig. 8b). The detailed assessments for the $GC_{1.0}$ + BMSC hydrogel group, including structural characteristics, freedom from degeneration changes in adjacent cartilage, the reconstitution of subchondral bone, hyaline cartilage and safrinin O staining, were significantly higher compared to the $GC_{1.0}$ and blank groups (Fig. 8c–g). It is noteworthy that a significant amount of cartilage-like tissue also formed in the bone defect area 6 weeks after hydrogel implantation, indicating that the hydrogel initially promoted cartilage formation, which is a crucial step in the bone healing process. This phenomenon may reflect the impact of biochemical and biophysical signals provided by the hydrogel on the differentiation fate of stem cells, particularly in favoring differentiation towards chondrocytes. Overall, these results confirmed the substantial facilitation of articular cartilage repair by $GC_{1.0}$ + BMSCs, highlighting its immense potential for cartilage tissue engineering.

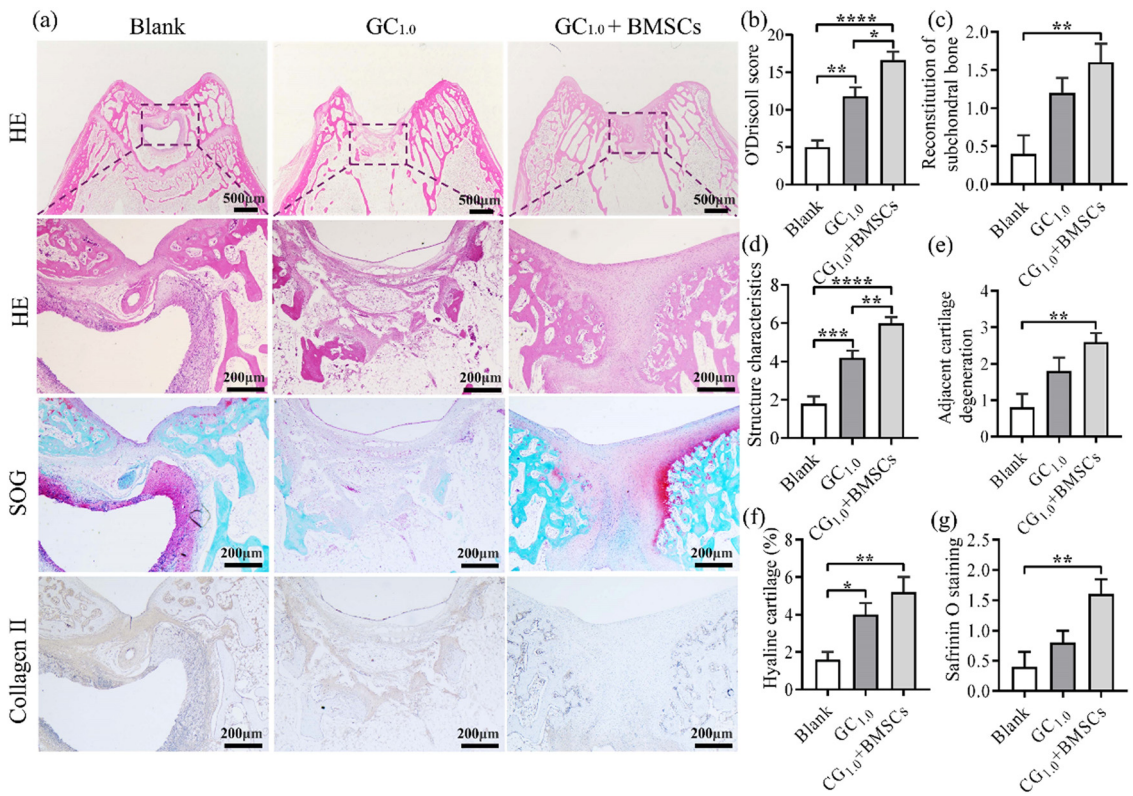

Fig. 8 Histological characterization of repaired cartilage. (a) The observation images of H&E, safranin-O/fast green (SOG), and Collagen-II stainings for cartilage defect repair. (b)–(g) Total score (b) and detail scoring content of the modified O'Driscoll score system, including reconstitution of subchondral bone (c), structural characteristics (d), freedom from degeneration changes in adjacent cartilage (e), hyaline cartilage (%) (f), and safrinin O staining (g). *$p < 0.05$, **$p < 0.01$, ***$p < 0.005$ and ****$p < 0.001$.

4. Conclusion

In summary, we have developed a novel cell adhesion-responsive hydrogel matrix for articular cartilage repair by combining gelatin methacrylate and chitosan methacrylate through photopolymerization. The hydrogel matrix allowed for precise control of the chemical microenvironment of the hydrogel matrix by adjusting the concentration of CHMA. The resulting hydrogels possessed fast gelation and bio-adaptable properties, including viscoelasticity, swelling, and controlled degradation *in vitro*. Furthermore, these hydrogels exhibited significant potential as a bioink for 3D bioprinting, enabling the creation of intricate and high-resolution constructs such as the femur, meniscus, and humerus, with a resolution as fine as 160 μm using suspension printing. More importantly, the hydrogel matrices presented biochemical cues that influenced the adhesion of BMSCs, leading to the formation of cell micro-aggregates and promoting chondrogenic differentiation. The differentiated cells showed increased expression of Sox9, Aggrecan, and Collagen 2a1 genes, as well as corresponding high protein expression both on the hydrogels and within the bioprinted scaffolds. These biocompatible and biodegradable hydrogels effectively repaired articular cartilage defects, exhibiting integration with surrounding tissues and resembling normal cartilage in terms of chondrocyte morphology and Collagen type II deposition. This innovative biomimetic cell adhesion-responsive hydrogel shows tremendous promise for cartilage tissue engineering.

Author contributions

Y. T. Liu and L. J. Du: conducting experiments, collecting data, administration, analysis and writing original draft. G. R. Li, Y. Luo, Z. M. Hu, R. Xu, Z. Y. Shi and Y. G. Chen: assisting with experimental operations, data curation and analysis. J. Yao, C. Zhang: Z. P. Jin, C. H. Zhang and C. C. Xie: software, data analysis and visualization. H. Zhang, J. Fu, Y. B. Zhu and Y. C. Zhu: project administration, funding acquisition, data verification, and writing and revising manuscript. All authors have read and agreed to the published version of the manuscript.

Conflicts of interest

The authors declare no conflict of interest.

Acknowledgements

This research was supported by the National Natural Science Foundation of China (22375225), the Medical and Health Science and Technology Program of Zhejiang Province (2021PY020, 2022KY1118), Traditional Chinese Medicine Science and Technology Program of Zhejiang Province (2023ZL154, 2024ZL894), Ningbo Natural Science Foundation (2021J257, 2022J121, 2023J141, 2023J159), and the Open Foundation of the State Key Laboratory of Molecular Engineering of Polymers (Fudan University) (K2024-35). Special thanks are given for the technical support received from the Core Facilities and Laboratory Animal Center, Health Science Center of Ningbo University.

References

1 Q. Yao, X. Wu, C. Tao, W. Gong, M. Chen, M. Qu, Y. Zhong, T. He, S. Chen and G. Xiao, *Signal Transduction Targeted Ther.*, 2023, **8**, 56.
2 A. Runer, R. Ossendorff, F. Öttl, V. A. Stadelmann, S. Schneider, S. Preiss, G. M. Salzmann and J. Hax, *Knee Surg Sports Traumatol Arthrosc*, 2023, **31**, 4977–4987.
3 S. J. MacDessi, S. Oussedik, M. P. Abdel, J. Victor, M. W. Pagnano and F. S. Haddad, *Bone Joint J.*, 2023, **105-b**, 102–108.
4 A. Y. Wong, D. Samartzis and C. Maher, *Lancet Rheumatol.*, 2023, **5**, e496–e497.
5 M. G. Siegel, J. H. Lubowitz, J. C. Brand and M. J. Rossi, *Arthroscopy*, 2021, **37**, 1359–1360.
6 D. K. Patel, E. Jung, S. Priya, S. Y. Won and S. S. Han, *Carbohydr. Polym.*, 2024, **323**, 121408.
7 L. Fu, L. Li, Q. Bian, B. Xue, J. Jin, J. Li, Y. Cao, Q. Jiang and H. Li, *Nature*, 2023, **618**, 740–747.
8 H. Zhang, S. Wu, W. Chen, Y. Hu, Z. Geng and J. Su, *Bioact. Mater.*, 2023, **23**, 156–169.
9 Y. Zhang, D. Li, Y. Liu, L. Peng, D. Lu, P. Wang, D. Ke, H. Yang, X. Zhu and C. Ruan, *The Innovation*, 2024, **5**, 100542.
10 D. Huang, Y. Li, Z. Ma, H. Lin, X. Zhu, Y. Xiao and X. Zhang, *Sci. Adv.*, 2023, **9**, eade9497.
11 S. Camarero-Espinosa, I. Beeren, H. Liu, D. B. Gomes, J. Zonderland, A. F. H. Lourenço, D. van Beurden, M. Peters, D. Koper, P. Emans, P. Kessler, T. Rademakers, M. B. Baker, N. Bouvy and L. Moroni, *Adv. Mater.*, 2024, e2310258.
12 M. C. Decarli, A. Seijas-Gamardo, F. L. C. Morgan, P. Wieringa, M. B. Baker, J. V. L. Silva, M. Moraes Â, L. Moroni and C. Mota, *Adv. Healthcare Mater.*, 2023, **12**, e2203021.
13 B. A. G. de Melo, Y. A. Jodat, S. Mehrotra, M. A. Calabrese, T. Kamperman, B. B. Mandal, M. H. A. Santana, E. Alsberg, J. Leijten and S. R. Shin, *Adv. Funct. Mater.*, 2019, **29**, 1906330.
14 N. D. Caprio, M. D. Davidson, A. C. Daly and J. A. Burdick, *Adv. Mater.*, 2024, e2312226.
15 R. E. Wilusz, J. Sanchez-Adams and F. Guilak, *Matrix Biol.*, 2014, **39**, 25–32.
16 D. Zhu, P. Trinh, E. Liu and F. Yang, *ACS Biomater. Sci. Eng.*, 2023, **9**, 831–843.
17 G. Le Saux, M. C. Wu, E. Toledo, Y. Q. Chen, Y. J. Fan, J. C. Kuo and M. Schvartzman, *ACS Appl. Mater. Interfaces*, 2020, **12**, 22399–22409.
18 H. Li, C. Wu, X. Yu and W. Zhang, *J. Mater. Res. Technol.*, 2023, **24**, 2279–2298.
19 Y. Luo, Y. Chen, Z. Gu, R. Ni, P. Feng, Z. Hu, L. Song, X. Shen, C. Gu, J. Li, T. Du, L. Yang, H. Zhang and Y. Zhu, *Mater. Today Bio*, 2023, **23**, 100853.

20 H. Wang, X. Li, M. Li, S. Wang, A. Zuo and J. Guo, *J. Adhes. Sci. Technol.*, 2022, **37**, 335–369.
21 B. D. Cosgrove, K. L. Mui, T. P. Driscoll, S. R. Caliari, K. D. Mehta, R. K. Assoian, J. A. Burdick and R. L. Mauck, *Nat. Mater.*, 2016, **15**, 1297–1306.
22 Q. Yang, J. Guo, S. Zhang, F. Guan, Y. Yu, S. Feng, X. Song, D. Bao and X. Zhang, *Int. J. Biol. Macromol.*, 2023, **236**, 124004.
23 P. Li, L. Fu, Z. Liao, Y. Peng, C. Ning, C. Gao, D. Zhang, X. Sui, Y. Lin, S. Liu, C. Hao and Q. Guo, *Biomaterials*, 2021, **278**, 121131.
24 B. S. Jang, K. H. Park, E. Y. Suh, B. S. Lee, S. W. Kang and K. M. Huh, *Int. J. Biol. Macromol.*, 2021, **187**, 955–963.
25 K. F. Yu, T. Y. Lu, Y. C. E. Li, K. C. Teng, Y. C. Chen, Y. Wei, T. E. Lin, N. C. Cheng and J. Yu, *Biomacromolecules*, 2022, **23**, 2814–2826.
26 X. Pang, X. He, Z. Qiu, H. Zhang, R. Xie, Z. Liu, Y. Gu, N. Zhao, Q. Xiang and Y. Cui, *Signal Transduction Targeted Ther.*, 2023, **8**, 1.
27 D. Wu, K. M. Yamada and S. Wang, *Annu. Rev. Cell Dev. Biol.*, 2023, **39**, 123–144.
28 M. Huber, J. Casares-Arias, R. Fässler, D. J. Müller and N. Strohmeyer, *Nat. Commun.*, 2023, **14**, 2143.
29 S. Guo, Y. Ren, R. Chang, Y. He, D. Zhang, F. Guan and M. Yao, *ACS Appl. Mater. Interfaces*, 2022, **14**, 34455–34469.
30 I. C. Lin, T. J. Wang, C. L. Wu, D. H. Lu, Y. R. Chen and K. C. Yang, *Regener. Ther.*, 2020, **14**, 238–244.
31 H. Wei, S. Yu, Y. Zhang, H. Zhang, Y. Ma, M. Xu, P. An, Y. Zhou, S. Halila, Y. Wei and J. Chen, *Carbohydr. Polym.*, 2023, **313**, 120904.
32 J. R. Yu, M. Janssen, B. J. Liang, H. C. Huang and J. P. Fisher, *Acta Biomater.*, 2020, **108**, 67–76.
33 E. M. Cruz, L. S. Machado, L. N. Zamproni, L. V. Bim, P. S. Ferreira, L. A. Pinto, L. A. Pessan, E. H. Backes and M. A. Porcionatto, *Pharmaceutics*, 2023, **15**(2), 627.
34 C. J. Liu, Q. F. Yu, Z. Q. Yuan, Q. P. Guo, X. T. Liao, F. Han, T. Feng, G. P. Liu, R. Z. Zhao, Z. Zhu, H. J. Mao, C. H. Zhu and B. Li, *Bioact. Mater.*, 2023, **25**, 445–459.
35 A. R. Osi, H. Zhang, J. Chen, Y. Zhou, R. Wang, J. Fu, P. Müller-Buschbaum and Q. Zhong, *ACS Appl. Mater. Interfaces*, 2021, **13**, 22902–22913.
36 J. Yang, Y. Liu, L. He, Q. Wang, L. Wang, T. Yuan, Y. Xiao, Y. Fan and X. Zhang, *Acta Biomater.*, 2018, **74**, 156–167.
37 K. Y. Zhang, Q. Feng, Z. W. Fang, L. Gu and L. M. Bian, *Chem. Rev.*, 2021, **121**(18), 11149–11193.
38 S. Taheri, H. S. Ghazali and Z. S. Ghazali, *et al.*, *Biomater. Res.*, 2023, **27**, 22.
39 R. Yang, W. L. Xue, X. B. Ma, Y. H. Ren, L. L. Xu, W. H. Kong, W. J. Zhang, P. H. Wang, X. Y. Tan and B. Chi, *Composites, Part B*, 2023, **250**, 110429.
40 J. Yang, H. He, D. Li, Q. Zhang, L. Xu and C. Ruan, *Bio-Des. Manuf.*, 2023, **6**, 586–608.
41 H. Zhang, Y. Luo, Z. Hu, M. Chen, S. Chen, Y. Yao, J. Yao, X. Shao, K. Wu, Y. Zhu and J. Fu, *Biofabrication*, 2024, **16**, 025009.
42 H. Zhang, Y. Cong, A. R. Osi, Y. Zhou, F. C. Huang, R. P. Zaccaria, J. Chen, R. Wang and J. Fu, *Adv. Funct. Mater.*, 2020, **30**(13), 1910573.
43 J. Chen, P. An, H. Zhang, Y. Zhang, H. Wei, Y. Zhou and Y. Zhu, *Biomed. Mater.*, 2022, **17**, 014106.
44 H. Y. Yeh, B. H. Liu and S. H. Hsu, *Biomaterials*, 2012, **33**, 8943–8954.
45 F. Guilak, R. J. Nims, A. Dicks, C. L. Wu and I. Meulenbelt, *Matrix Biol.*, 2018, **71–72**, 40–50.

